

# Beyond Single-Shot Fidelity: Chernoff-Based Throughput Optimization in Superconducting Qubit Readout

Sinan Bugu<sup>1,2,\*</sup>

<sup>1</sup>*Department of Physics and Astronomy, North Carolina State University, Raleigh, North Carolina, USA*

<sup>2</sup>*BuQuLab Research Laboratory, Winston-Salem, North Carolina, USA*

(Dated: February 27, 2026)

Single-shot fidelity is the standard benchmark for superconducting qubit readout, but it does not directly minimize the total wall-clock time required to certify a quantum state. We develop an information-theoretic description of dispersive readout by treating the measurement record as a stochastic communication channel. Within a trajectory model that incorporates  $T_1$  relaxation with full cavity memory, we compute the classical Chernoff information governing the multi-shot error exponent. We find a consistent separation between the integration time that maximizes single-shot fidelity and the time that minimizes total certification time. For representative transmon parameters and hardware overheads, the throughput-optimal integration window is longer than the fidelity-optimal one, yielding certification speedups of approximately 9–11%, with the gain saturating near  $1.13\times$  in the high-readout-power and high-overhead regime. Comparing the extracted classical information to the unit-efficiency Gaussian Chernoff benchmark defines an information-extraction efficiency metric. Typical dispersive schemes are limited to  $\sim 45\%$  capture at short integration times by detection efficiency, decreasing to  $\eta_{\text{info}}(\tau_{\text{rate}}) \approx 12\%$  at  $\tau_{\text{rate}} \approx 1.22 \mu\text{s}$  due to  $T_1$ -induced trajectory smearing. This formulation connects readout calibration to the operational objective of minimizing certification time in high-throughput superconducting processors.

Keywords: Superconducting qubits, Dispersive readout, Chernoff error exponent, Quantum hypothesis testing, Readout calibration, Throughput optimization, Transmon

## I. INTRODUCTION

The scaling of superconducting quantum processors toward the fault-tolerant regime requires not only high-fidelity operations but also high-throughput certification cycles [1, 2]. Recent surface-code demonstrations have shown that cycle time is a critical scaling bottleneck [3, 4], with system-level latencies in large-scale processors often dominating total execution time [5]. Within the circuit quantum electrodynamics (cQED) architecture, dispersive readout of transmon qubits remains one of the most persistent performance constraints [6, 7], despite advances in dynamic control of the dispersive interaction that push readout speed and fidelity [8]. Although coherent gates now operate on nanosecond timescales, measurement windows remain disproportionately long relative to intrinsic device dynamics [9, 10].

This latency reflects a trade-off inherent to dispersive measurement. Increasing the measurement drive to accelerate information extraction enhances measurement-induced dephasing, AC Stark shifts, and transitions into non-computational leakage manifolds [11–14]. At sufficiently high drive powers, these effects can escalate into nonlinear phenomena such as transmon ionization [15] and stochastic state transitions arising from breakdown of the dispersive approximation [16]. Alternative coupling architectures have therefore been explored to enable faster measurement while mitigating backaction, including longitudinal interaction schemes [17] and the quar-

ton coupler enabling nanosecond-scale readout windows [18]. Complementary mitigation strategies, such as integrated filtering and Purcell-protected device designs, further suppress measurement-induced decay and enhance stability in high-power regimes [19].

In standard practice, readout is optimized by maximizing single-shot Bayes fidelity [20]. More recently, model-based approaches have enabled systematic suppression of assignment and leakage errors in multi-qubit architectures [21]. However, for protocols involving repeated measurements, single-shot fidelity does not fully capture the cumulative effects of leakage and hardware latency [22]. While multiplexed readout [23, 24], active reset [25], and near-quantum-limited amplification [26, 27] have improved raw measurement performance, scalable architectures ultimately seek to minimize the wall-clock time required to reach a target confidence level  $\epsilon$ . As emphasized in decentralized coordination and certification studies [28, 29], this objective naturally shifts optimization from isolated decision accuracy toward certification throughput. Consequently, the fidelity-optimal integration time  $\tau_{\text{fid}}$  may be suboptimal once hardware latency and reset constraints are incorporated [30].

Here we evaluate readout through an information-theoretic lens, treating measurement score distributions as probability objects rather than isolated binary outcomes [29, 31]. The role of Chernoff information as a figure of merit for qubit readout has been established [32], with asymptotic optimality grounded in hypothesis testing theory [33, 34]. Prior work, however, has primarily addressed repetitive measurement statistics in platform-agnostic settings. Here we apply this perspective to continuous-time dispersive transmon readout with

\* sbugu@ncsu.edu; sinanbugu@gmail.com

stochastic  $T_1$  relaxation and explicit hardware latency.

Our central contribution is to formulate readout calibration as a wall-clock certification problem. Rather than maximizing single-shot fidelity, we minimize the total certification time

$$T_{\text{cert}}(\tau) = \frac{\log(1/\epsilon)}{C(\tau)}(\tau + \tau_{\text{oh}}), \quad (1)$$

which incorporates both the classical Chernoff information  $C(\tau)$  and the fixed per-shot overhead  $\tau_{\text{oh}}$ . Consistent with experimental observations [7, 20], we model homodyne score distributions using Gaussian noise kernels, subsequently deformed by  $T_1$  relaxation events that produce asymmetric tails and assignment errors [10]. Using a trajectory model with full cavity memory [35], we demonstrate a systematic separation between the fidelity-optimal integration time  $\tau_{\text{fid}}$  and the throughput-optimal time  $\tau_{\text{rate}}$ , a separation that persists even in the long-coherence limit.

Beyond numerical optimization, we derive asymptotic scaling laws showing that any nonzero hardware overhead shifts the throughput optimum toward longer integration times to amortize fixed temporal costs. We further introduce an experimentally accessible diagnostic by benchmarking classical Chernoff capture against an ideal Gaussian Chernoff benchmark [36, 37]. Jointly, these results define a calibration procedure for high-duty-cycle superconducting processors, where power-induced deviations from the dispersive regime [38] require careful optimization of temporal resources. Recent efforts to engineer photon-noise-tolerant readout mechanisms further highlight the interplay between speed, noise, and nonlinearity in dispersive measurement [39].

## II. STOCHASTIC COMMUNICATION MODEL OF DISPERSIVE READOUT

### A. Dispersive Dynamics and Homodyne SNR

We model the dispersive readout of a transmon qubit coupled to a readout resonator, described by the Hamiltonian  $H/\hbar = \omega_r a^\dagger a + \frac{\omega_q}{2} \sigma_z + \chi a^\dagger a \sigma_z$  [40]. Under a constant microwave drive, the displacement of the cavity coherent states  $|\pm \alpha(t)\rangle$  depends on the qubit state. The separation between these states along the measured quadrature grows according to the cavity response function:

$$\Delta\alpha(t) = \frac{4\chi}{\kappa} \left(1 - e^{-\kappa t/2}\right) \quad (2)$$

where  $\chi$  is the dispersive shift and  $\kappa$  is the cavity linewidth [10].

The information reaching the homodyne detector is processed via a matched filter to maximize the signal-to-noise ratio (SNR) [9, 35]. The filter weighting  $h(t)$  is chosen to match the expected signal shape  $h(t) = \Delta\alpha(t)$ .

For a given integration time  $\tau$ , the squared signal-to-noise ratio ( $SNR^2$ ) at the detector is:

$$SNR^2(\tau) = \eta\kappa\bar{n} \int_0^\tau |\Delta\alpha(t)|^2 dt \quad (3)$$

where  $\eta$  is the overall quantum efficiency and  $\bar{n}$  is the steady-state photon number. We define the matched-filter score as a normalized projection variable whose conditional noise variance is unity. In this convention, detector inefficiency  $\eta$  enters exclusively through the mean separation encoded in  $SNR(\tau)$ , while the additive noise variance of the score distribution is fixed to one. As established in the characterization of NISQ-era resources, the statistical structure of these distributions determines the persistence of quantum signatures under noise [41, 42]. While we assume a standard homodyne detection chain, alternative high-efficiency detection schemes using on-chip microwave photon counters have demonstrated comparable performance by mapping quantum information directly into binary click statistics [43].

### B. Stochastic Trajectory Smearing with Cavity Memory

To accurately represent the excited state distribution  $p_e(x)$ , we must account for the stochastic relaxation of the qubit from  $|e\rangle$  to  $|g\rangle$  at a jump time  $t_j \in [0, \tau]$ . We adopt a trajectory model that ensures continuity of the cavity field at the jump time. For  $t < t_j$ , the system follows the excited-state trajectory  $\alpha(t) = +\Delta\alpha(t)$ . At the moment of the jump, the cavity field is at  $+\Delta\alpha(t_j)$ . For  $t > t_j$ , it relaxes exponentially toward the ground-state trajectory  $-\Delta\alpha(t)$  at a rate governed by  $\kappa/2$ :

$$\alpha(t > t_j) = -\Delta\alpha(t) + 2\Delta\alpha(t_j)e^{-\kappa(t-t_j)/2} \quad (4)$$

This expression guarantees continuity at the jump boundary,  $\alpha(t_j^-) = \alpha(t_j^+) = \Delta\alpha(t_j)$ . We assume that the readout drive remains on throughout the integration window, so after a decay event the cavity relaxes toward the driven ground-state trajectory rather than the undriven vacuum. The matched-filter score  $s(t_j)$  is then calculated by projecting this continuous trajectory onto the filter  $h(t)$ . The full excited state distribution is constructed as:

$$p_e(x) = e^{-\tau/T_1} \mathcal{N}(\mu_e, 1) + \int_0^\tau \frac{1}{T_1} e^{-t_j/T_1} \mathcal{N}(\mu(t_j), 1) dt_j \quad (5)$$

where the first term accounts for trajectories where no decay occurs during the integration window.

### C. Certification Wall-Clock Time Objective

Building on the information-theoretic perspective developed in [28, 29], we formulate certification as a binary

hypothesis test between  $p_g(x)$  and  $p_e(x)$ . Distinguishability is quantified using the classical Chernoff information [33, 44]:

$$C = -\log \left( \min_{s \in [0,1]} \int p_g(x)^s p_e(x)^{1-s} dx \right) \quad (6)$$

The ultimate objective is to minimize the total wall-clock time required to certify the qubit state to a target error probability  $\epsilon$ . Incorporating the hardware-specific overhead  $\tau_{\text{oh}}$ , which accounts for latencies and reset times [3, 4], the total certification time is:

$$T_{\text{cert}}(\tau) = \frac{\log(1/\epsilon)}{C(\tau)} (\tau + \tau_{\text{oh}}) \quad (7)$$

The Chernoff information characterizes the asymptotic large-shot error exponent. For the target error levels considered here, the required number of repetitions can be modest; we therefore use  $C(\tau)$  as a throughput proxy and focus on the location of the certification-time minimum rather than finite-sample corrections to the exponent. We numerically minimize  $T_{\text{cert}}(\tau)$  to find the throughput-optimal integration time  $\tau_{\text{rate}}$ . This is compared to the fidelity-optimal time  $\tau_{\text{fid}}$ , obtained by maximizing  $F = 1 - \frac{1}{2} \int \min(p_g, p_e) dx$ , to determine the speedup factor:

$$\text{Speedup} = \frac{T_{\text{cert}}(\tau_{\text{fid}})}{T_{\text{cert}}(\tau_{\text{rate}})} \quad (8)$$

This metric quantifies the advantage of an information-theoretic approach over standard single-shot optimization in the presence of realistic constraints [28, 29]. Following the diagnostic approach developed for multi-agent coordination [29], we isolate the physical degradation of the measurement channel by defining a unit-efficiency Gaussian Chernoff benchmark

$$C_{\text{ideal}}(\tau) = \frac{1}{8} \kappa \bar{n} \int_0^\tau |\Delta\alpha(t)|^2 dt, \quad (9)$$

which corresponds to the classical Chernoff information in the absence of  $T_1$  relaxation and with detection efficiency  $\eta = 1$ . This benchmark represents the ideal distinguishability limit for a homodyne receiver observing a non-decaying qubit ( $T_1 \rightarrow \infty$ ), and provides a baseline against which we quantify the information loss attributable to detector inefficiency and  $T_1$ -induced trajectory smearing. All reported curves are obtained from deterministic numerical integration of the score distributions without stochastic sampling. Convergence with respect to discretization of the score grid, time grid, and decay-time quadrature was verified, and residual numerical errors are smaller than the marker size in all figures.

#### D. Asymptotic Scaling and Overhead-Induced Shift

To clarify the structural origin of the systematic separation between  $\tau_{\text{fid}}$  and  $\tau_{\text{rate}}$ , we consider the long-coherence limit ( $T_1 \rightarrow \infty$ ) where the matched-filter

score distributions remain symmetric Gaussians. In this regime, the classical Chernoff information reduces to

$$C(\tau) = \frac{\text{SNR}^2(\tau)}{8}. \quad (10)$$

The throughput objective (7) is therefore equivalent, up to a constant prefactor, to minimizing

$$T_{\text{cert}}(\tau) \propto \frac{\tau + \tau_{\text{oh}}}{\text{SNR}^2(\tau)}. \quad (11)$$

A stationary point satisfies the exact condition

$$\begin{aligned} \frac{d}{d\tau} \left( \frac{\tau + \tau_{\text{oh}}}{\text{SNR}^2(\tau)} \right) &= 0 \\ \iff \text{SNR}^2(\tau) &= (\tau + \tau_{\text{oh}}) \frac{d}{d\tau} \text{SNR}^2(\tau). \end{aligned} \quad (12)$$

For dispersive readout with finite resonator linewidth,  $\text{SNR}^2(\tau)$  is not perfectly linear in  $\tau$  because of cavity ring-up. Using the cavity response  $\Delta\alpha(t) \propto (1 - e^{-\kappa t/2})$ , the integrand entering  $\text{SNR}^2(\tau) \propto \int_0^\tau \Delta\alpha(t)^2 dt$  contains both  $e^{-\kappa t/2}$  and  $e^{-\kappa t}$  terms, producing an initially sublinear growth that crosses over to an asymptotically linear regime at long times. This early-time curvature regularizes the optimization and yields a well-defined interior minimum of  $T_{\text{cert}}(\tau)$ .

It is instructive to contrast this with a purely linear surrogate  $\text{SNR}^2(\tau) \approx a\tau + b$  valid only deep in the steady-state regime. Substituting this form gives

$$T_{\text{cert}}(\tau) \propto \frac{\tau + \tau_{\text{oh}}}{a\tau + b}, \quad \frac{dT_{\text{cert}}}{d\tau} \propto \frac{b - a\tau_{\text{oh}}}{(a\tau + b)^2}, \quad (13)$$

which is monotonic in  $\tau$  and therefore cannot by itself produce an interior optimum. The existence and location of  $\tau_{\text{rate}}$  thus depend on the finite ring-up dynamics captured by the full cavity-memory model.

Equation (12) also makes the overhead-induced shift transparent. Increasing  $\tau_{\text{oh}}$  increases the right-hand side and therefore pushes the solution  $\tau_{\text{rate}}$  toward larger integration times, reflecting an amortization effect: when fixed temporal costs are nonzero, it becomes advantageous to extract more information per shot. This establishes that the rightward shift of the throughput-optimal integration time is not a decoherence-induced artifact, but a structural consequence of optimizing wall-clock certification time even in the  $T_1 \rightarrow \infty$  limit. In practice, the crossover between the ring-up and linear regimes of  $\text{SNR}^2(\tau)$  can produce two competing local minima at very small overheads; for the physically relevant range  $\tau_{\text{oh}} \gtrsim 5 \mu\text{s}$  the global minimum is unique and shifts monotonically with overhead.

### III. RESULTS

We evaluate the performance of the information-theoretic optimization framework using parameters representative of contemporary superconducting circuit architectures: a dispersive shift  $\chi/2\pi = 1.2 \text{ MHz}$ , cavity

linewidth  $\kappa/2\pi = 5.0$  MHz, and an average steady-state photon number  $\bar{n} = 80$ . Unless otherwise stated, we assume a detection efficiency  $\eta = 0.45$  and a qubit relaxation time  $T_1 = 30 \mu\text{s}$ . Dispersive shifts in the MHz range and cavity linewidths of several MHz are routinely reported in high-fidelity readout experiments [7, 20]. Average photon numbers  $\bar{n} \sim 50\text{--}100$  and measurement efficiencies  $\eta \approx 0.4\text{--}0.6$  are consistent with modern high-efficiency readout implementations [11, 45], while relaxation times  $T_1 \sim 20\text{--}50 \mu\text{s}$  are typical of contemporary transmon platforms [46].

The assumed per-shot overhead  $\tau_{\text{oh}} = 15 \mu\text{s}$  is treated as a lumped system-level latency parameter incorporating classical control processing, resonator depletion, and reset timing constraints. Experimental studies of active resonator reset and measurement-feedback cycles demonstrate that cavity depletion and control-flow latency can occupy a substantial fraction of the measurement cycle, particularly in architectures prioritizing Purcell protection and coherence [30, 47]. While optimized fast-reset protocols can reduce this overhead, realistic superconducting control stacks commonly retain microsecond-scale latencies, motivating the inclusion of an explicit  $\tau_{\text{oh}}$  term in throughput analysis.

### A. Information Accumulation and Trajectory Smearing

The dynamics of information accumulation are determined by the cavity response and the subsequent smearing of score distributions due to qubit decay. Figure 1(a) shows the growth of the cavity state separation  $\Delta\alpha(t)$ , which approaches its steady-state value on a timescale governed by  $\kappa^{-1}$ . The integrated information, quantified by the squared signal-to-noise ratio  $SNR^2(\tau)$ , scales nonlinearly during the ring-up phase before entering a linear growth regime [Fig. 1(b)]. At  $\tau = 1.0 \mu\text{s}$ , the resulting score distributions  $p_g(x)$  and  $p_e(x)$  are clearly separated, though  $p_e(x)$  exhibits a characteristic tail extending toward the ground-state mean due to  $T_1$  events [Fig. 1(c)].

One consequence of this  $T_1$ -induced smearing is the introduction of asymmetry between the hypotheses. Figure 2(a) compares the excited state distribution with and without relaxation; the decay events effectively "pollute" the excited state manifold, shifting the optimal Chernoff parameter  $s^*$  away from the symmetric Gaussian value of 0.5 [Fig. 2(b)]. As  $\tau$  increases,  $s^*$  drops sharply, indicating that the optimal classifier becomes increasingly biased against assigning the excited state to scores that could have resulted from a decay event.

We quantify the quality of the measurement scheme via the information extraction efficiency  $\eta_{\text{info}}$ , defined as the ratio of the classical Chernoff information  $C(\tau)$  to the unit-efficiency Gaussian benchmark  $C_{\text{ideal}}(\tau)$ . As shown in Fig. 2(c), the efficiency reaches its maximum value of 45% at short integration times, reflecting the finite detection efficiency  $\eta$ . As  $\tau$  increases, the accumulated prob-

ability of  $T_1$  relaxation events causes the classical information to deviate from the ideal Gaussian scaling, with the extraction efficiency falling to approximately 12% at the throughput-optimal integration point.

### B. Separation of Optimal Integration Times

The main observation is the systematic separation between the integration time that maximizes single-shot fidelity,  $\tau_{\text{fid}}$ , and the time that minimizes total certification time,  $\tau_{\text{rate}}$ . Figure 3 illustrates this effect for standard parameters. While the Bayes fidelity peaks at  $\tau_{\text{fid}} \approx 0.78 \mu\text{s}$ , the total wall-clock certification time required to reach an error threshold  $\epsilon = 10^{-4}$  attains its minimum at a significantly longer integration time,  $\tau_{\text{rate}} \approx 1.22 \mu\text{s}$ .

This shift arises because the certification time  $T_{\text{cert}}$  accounts for both the information rate  $C(\tau)$  and the fixed hardware overhead. In the throughput-optimal regime, it is more efficient to integrate for longer—thereby extracting more information per shot and reducing the total number of required shots—than to maximize single-shot fidelity. For the baseline parameters, this throughput optimization yields a speedup of  $1.11\times$  compared to operating at the fidelity-optimal point.

### C. Scaling and Global Performance Limits

The magnitude of the speedup depends on the interplay between qubit coherence and hardware constraints. Figure 4(a) maps the speedup factor across a range of  $T_1$  times and detection efficiencies  $\eta$ . At fixed measurement efficiency, longer  $T_1$  produces a modest increase in speedup, although the dependence on  $T_1$  is weaker than the dependence on  $\eta$  or the per-shot overhead. This reflects the fact that longer coherence reduces decay-induced asymmetry, allowing more efficient information accumulation per shot.

To estimate the maximum achievable gain of this optimization, we performed an extensive sweep over the photon number  $\bar{n}$  and hardware overhead [Fig. 4(b)]. The speedup increases with both parameters, reaching a maximum of approximately  $1.13\times$  at  $\bar{n} = 120$  and an overhead of  $30 \mu\text{s}$ . This confirms that while the gains are modest (typically 7–14%), they are consistent across the physically reachable parameter space of current transmon systems.

### D. Consistency in the Gaussian Limit

We validate the numerical framework by examining the limit of infinite qubit coherence ( $T_1 \rightarrow \infty$ ). In this regime, the score distributions remain symmetric Gaussians. Figure 5(a) shows that the numerically computed

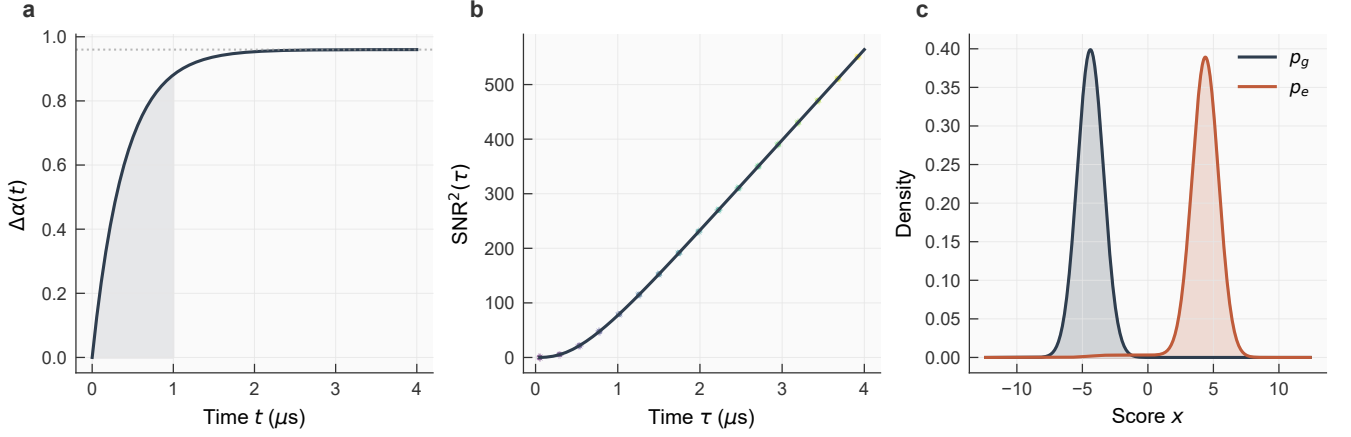


FIG. 1. **Dynamics of information accumulation in dispersive readout.** (a) Temporal evolution of the cavity coherent state separation  $\Delta\alpha(t)$  following the onset of the drive pulse. The separation approaches the steady-state limit of  $4\chi/\kappa$  as the resonator field rings up. (b) Integrated signal-to-noise ratio squared ( $SNR^2$ ) as a function of integration time  $\tau$ . The initial quadratic growth reflects the cavity ring-up phase, transitioning to a linear regime as the steady-state signal power is reached. (c) Score distributions  $p_g(x)$  and  $p_e(x)$  at  $\tau = 1.0 \mu s$ . While the ground state is nearly Gaussian, the excited state distribution exhibits a tail extending toward the ground-state mean, a direct consequence of  $T_1$  relaxation events occurring during the measurement window.

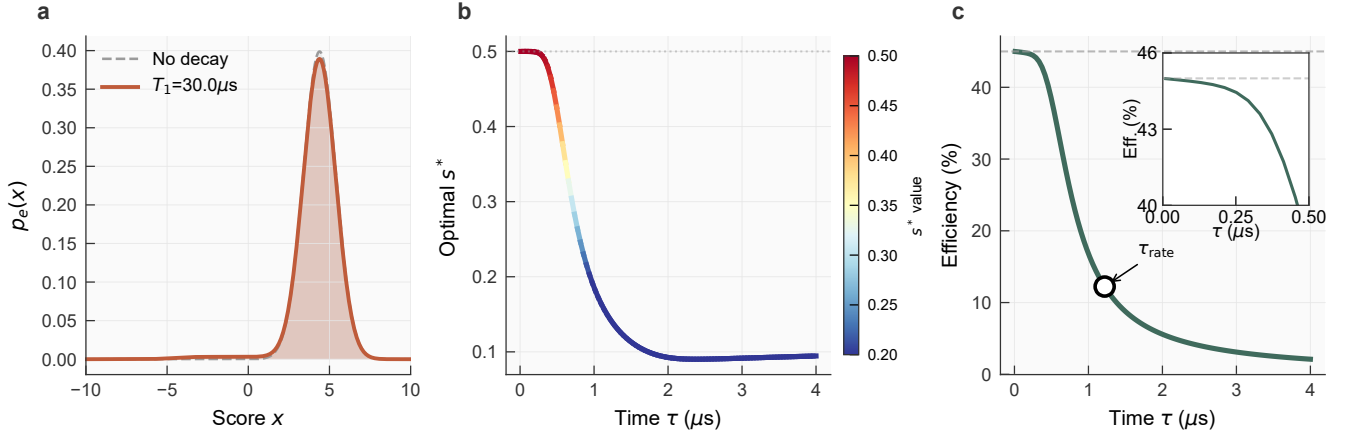


FIG. 2. **Characterizing  $T_1$ -induced asymmetry and extraction efficiency.** (a) Comparison of the excited-state score distribution  $p_e(x)$  in the ideal limit (no decay) and the realistic regime ( $T_1 = 30 \mu s$ ). The relaxation events "pollute" the score manifold, significantly shifting the optimal decision threshold. (b) The optimal Chernoff parameter  $s^*$  as a function of integration time. At short  $\tau$ , the distributions remain nearly symmetric ( $s^* \approx 0.5$ ), but as decay events accumulate,  $s^*$  shifts toward zero, indicating that the optimal classifier becomes more biased against the excited state. (c) Information extraction efficiency  $\eta_{\text{info}}$  relative to the unit-efficiency Gaussian Chernoff benchmark. The efficiency reaches its theoretical maximum of 45% (limited by detection efficiency  $\eta$ ) at short integration times and diminishes monotonically as  $\tau$  increases, reflecting the progressive information loss driven by stochastic  $T_1$  relaxation during the measurement window.

Chernoff information  $C$  agrees with the analytical Gaussian result  $SNR^2/8$ , confirming the internal consistency of the discretized integration procedure.

Figure 5(b) demonstrates that a separation between  $\tau_{\text{fid}}$  and  $\tau_{\text{rate}}$  persists even in the  $T_1 \rightarrow \infty$  limit. This separation reflects the difference between the single-shot Bayes-fidelity objective and the multi-shot Chernoff error-exponent objective. Increasing the hardware overhead  $\tau_{\text{oh}}$  further amplifies this effect over the physically

relevant range.

Together, these results confirm that the observed systematic separation is a structural property of the certification objective, rather than an artifact of qubit relaxation.

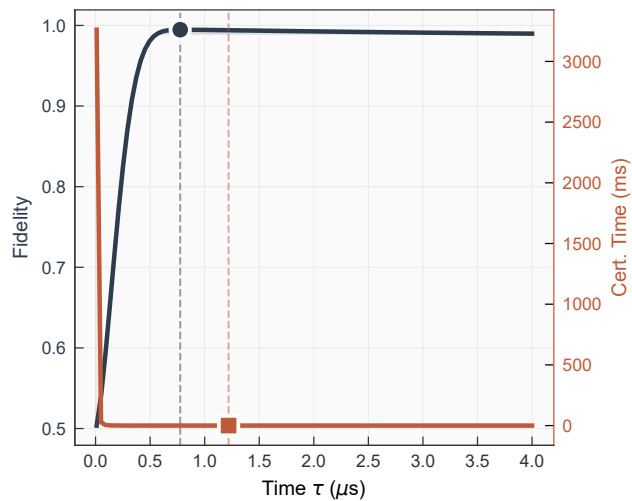


**FIG. 3. Systematic separation between fidelity and certification-time optima.** The Bayes fidelity (primary axis) and total wall-clock certification time (secondary axis) are plotted against integration time  $\tau$  for a target error  $\epsilon = 10^{-4}$ . Vertical dashed lines (with corresponding markers) indicate the fidelity-optimal point ( $\tau_{\text{fid}}$ ) and the certification-optimal point ( $\tau_{\text{rate}}$ ). The minimum in certification time occurs at a noticeably longer integration window, demonstrating that throughput optimization involves a fundamental trade-off between single-shot confidence and per-shot hardware overhead.

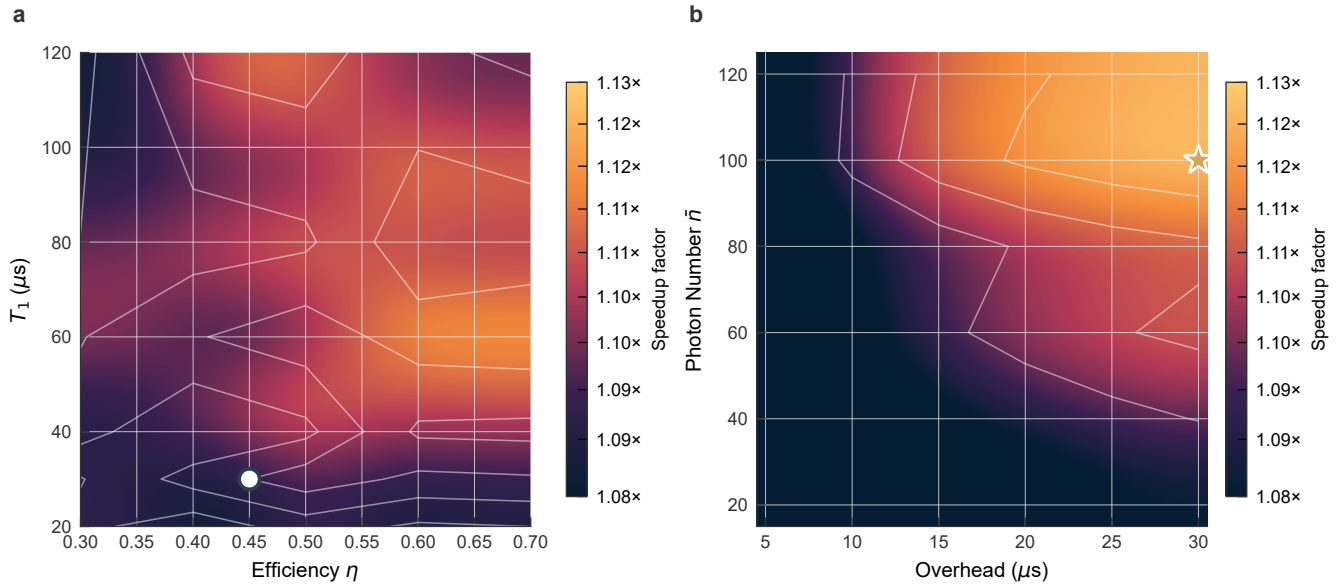


FIG. 4. **Scaling of certification speedup across parameter space.** (a) Speedup factor as a function of qubit relaxation time  $T_1$  and detection efficiency  $\eta$ . Higher efficiencies allow the measurement to reach the certification threshold more rapidly, making the fixed hardware overhead the dominant bottleneck. The white circle marks the baseline parameters ( $T_1 = 30$   $\mu\text{s}$ ,  $\eta = 0.45$ ) used throughout this work. (b) Speedup factor as a function of steady-state photon number  $\bar{n}$  and per-shot hardware overhead. The gold star indicates the maximum speedup of approximately  $1.13\times$  achieved at  $\bar{n} = 120$  and 30  $\mu\text{s}$  overhead, representing the performance ceiling in the high-power, high-overhead regime.

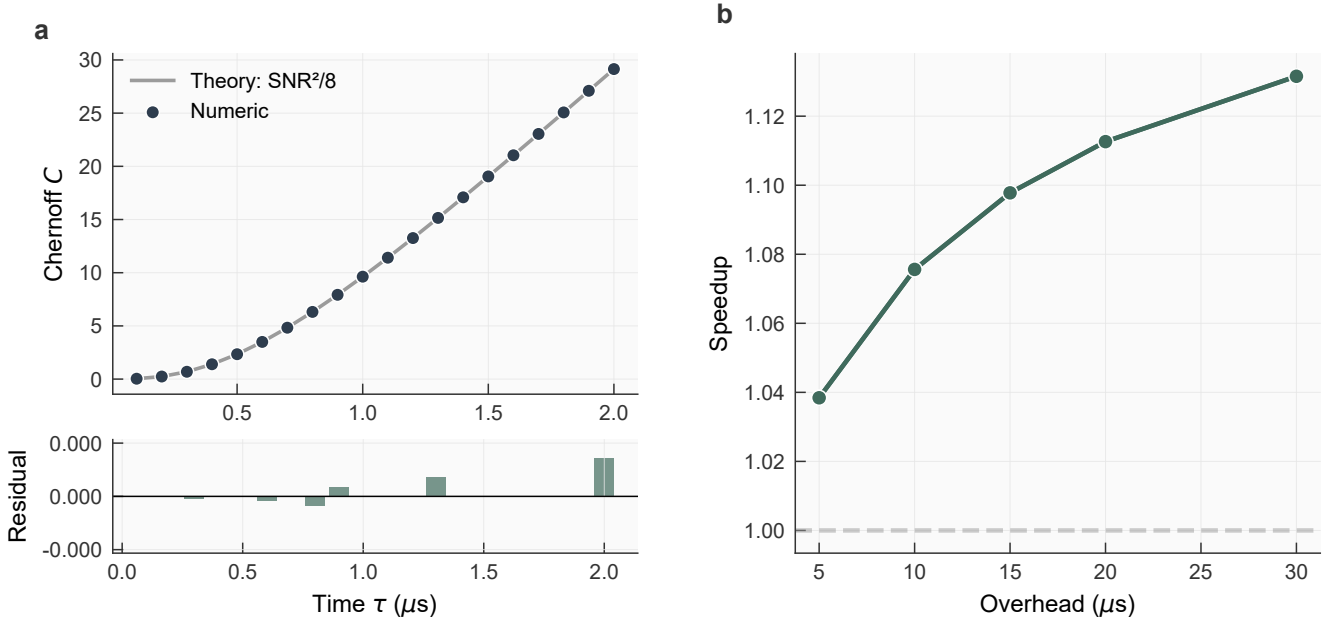


FIG. 5. **Framework validation and the Gaussian limit.** (a) Calculated Chernoff information  $C$  (points) compared to the analytical  $SNR^2/8$  limit (line) in the absence of qubit decay ( $T_1 \rightarrow \infty$ ). The lower panel shows residuals ( $C_{\text{num}} - C_{\text{theory}}$ ), confirming excellent agreement and numerical stability. (b) Speedup factor versus per-shot overhead in the  $T_1 \rightarrow \infty$  limit. The overhead axis begins at 5  $\mu\text{s}$ , since zero overhead is unphysical in realistic control stacks. Over this range the speedup increases monotonically with overhead, consistent with the amortization argument of Sec. II.D: the throughput optimum  $\tau_{\text{rate}}$  shifts to longer integration times while the fidelity optimum  $\tau_{\text{fid}}$  is overhead-independent.

#### IV. CONCLUSION

The optimization of dispersive readout has traditionally been treated as a problem of maximizing single-shot distinguishability. However, we find that single-shot fidelity is not the correct objective when the operational goal is to minimize total wall-clock certification time in a high-duty-cycle processor. By framing readout as a stochastic communication channel and optimizing the Chernoff error exponent directly, we identify a systematic separation between the fidelity-optimal integration time  $\tau_{\text{fid}}$  and the throughput-optimal time  $\tau_{\text{rate}}$ .

This systematic separation is not merely a consequence of qubit relaxation. Our asymptotic analysis in the long-coherence Gaussian limit demonstrates that any nonzero per-shot hardware overhead  $\tau_{\text{oh}}$  structurally shifts the throughput optimum toward longer integration times. Physically, this reflects an amortization effect: it is advantageous to extract more information per shot when fixed temporal costs dominate. Qubit relaxation during the measurement window further amplifies the asymmetry of score distributions, modifying the Chernoff geometry and strengthening the separation between optima.

For representative transmon parameters, we find that integrating approximately 50% longer than the fidelity-

optimal time yields a reduction of roughly 9–11% in total certification runtime. While the achievable speedup is bounded (with an observed ceiling near  $1.13\times$  in realistic parameter regimes), it represents a calibration-level improvement requiring no hardware modification.

Benchmarking classical Chernoff extraction against the unit-efficiency Gaussian Chernoff benchmark, we introduce an experimentally accessible diagnostic for quantifying information loss. The marked drop in extraction efficiency at the throughput-optimal integration time highlights the distinct roles of amplifier inefficiency and  $T_1$ -induced trajectory smearing in limiting operational performance.

As superconducting processors scale and repetition rates increase, readout and reset latency will become increasingly dominant contributors to runtime. This analysis reframes measurement calibration in terms of wall-clock certification time, aligning readout optimization with the operational objective of large-scale quantum processors.

#### CODE AVAILABILITY

The numerical code used to generate all figures and data in this study will be made available upon publication.

- 
- [1] A. G. Fowler, M. Mariantoni, J. M. Martinis, and A. N. Cleland, Surface codes: Towards practical large-scale quantum computation, *Physical Review A* **86**, 032324 (2012).
  - [2] B. M. Terhal, Quantum error correction for quantum memories, *Reviews of Modern Physics* **87**, 307 (2015).
  - [3] R. Acharya and others (Google Quantum AI), Quantum error correction below the surface code threshold, *Nature* **638**, 920 (2025), demonstrates surface code operation where readout cycle time is the critical throughput metric.
  - [4] S. Krinner, N. Lacroix, A. Remm, A. Di Paolo, E. Genois, C. Leroux, C. Hellings, S. Lazar, F. Swiadek, J. Herrmann, *et al.*, Realizing repeated quantum error correction in a distance-three surface code, *Nature* **605**, 669 (2022).
  - [5] F. Arute *et al.*, Quantum supremacy using a programmable superconducting processor, *Nature* **574**, 505 (2019).
  - [6] A. Blais, A. L. Grimsmo, S. M. Girvin, and A. Wallraff, Circuit quantum electrodynamics, *Reviews of Modern Physics* **93**, 025005 (2021).
  - [7] T. Walter, P. Kurpiers, S. Gasparinetti, P. Magnard, A. Potočnik, Y. Salathé, M. Pechal, M. Mondal, M. Oppliger, C. Eichler, and A. Wallraff, Rapid high-fidelity single-shot dispersive readout of superconducting qubits, *Physical Review Applied* **7**, 054020 (2017).
  - [8] F. Swiadek, R. Shillito, P. Magnard, *et al.*, Enhancing dispersive readout of superconducting qubits through dynamic control of the dispersive shift: Experiment and theory, *PRX Quantum* **5**, 040326 (2024).
  - [9] A. A. Clerk, M. H. Devoret, S. M. Girvin, F. Marquardt, and R. J. Schoelkopf, Introduction to quantum noise, measurement, and amplification, *Reviews of Modern Physics* **82**, 1155 (2010).
  - [10] J. Gambetta, A. Blais, M. Boissonneault, A. A. Houck, D. Schuster, and S. M. Girvin, Quantum trajectory approach to circuit qed: Quantum jumps and the zeno effect, *Phys. Rev. A* **77**, 012112 (2008).
  - [11] M. D. Reed, L. DiCarlo, B. Johnson, L. Sun, D. Schuster, L. Frunzio, and R. Schoelkopf, High-fidelity readout in circuit quantum electrodynamics using the jaynes-cummings nonlinearity, *Physical review letters* **105**, 173601 (2010).
  - [12] K. W. Murch, S. Weber, C. Macklin, and I. Siddiqi, Observing single quantum trajectories of a superconducting quantum bit, *Nature* **502**, 211 (2013).
  - [13] M. Hatridge, S. Shankar, M. Mirrahimi, F. Schackert, K. Geerlings, T. Brecht, K. Sliwa, B. Abdo, L. Frunzio, S. M. Girvin, *et al.*, Quantum back-action of an individual variable-strength measurement, *Science* **339**, 178 (2013).
  - [14] M. Féchant, M. F. Dumas, D. Bénâtre, N. Gosling, P. Lenhard, M. Spiecker, S. Geisert, S. Ihssen, W. Wernsdorfer, B. D’Anjou, *et al.*, Offset charge dependence of measurement-induced transitions in transmons, *Physical Review Letters* **135**, 180603 (2025).
  - [15] M. F. Dumas, B. Groleau-Paré, A. McDonald, M. H. Muñoz-Arias, C. Lledó, B. D’Anjou, and A. Blais, Measurement-induced transmon ionization, *Physical Re-*

- view X **14**, 041023 (2024), detailed study of high-power readout failure modes.
- [16] K. N. Nesterov and I. V. Pechenezhskiy, Measurement-induced state transitions in dispersive qubit-readout schemes, *Physical Review Applied* **22**, 064038 (2024).
- [17] N. Didier, J. Bourassa, and A. Blais, Fast quantum non-demolition readout by parametric modulation of longitudinal qubit-oscillator interaction, *Physical review letters* **115**, 203601 (2015).
- [18] Y. Ye, J. B. Kline, S. Chen, A. Yen, and K. P. O'Brien, Ultrafast superconducting qubit readout with the qurton coupler, *Science Advances* **10**, eado9094 (2024), proposes a non-dispersive coupling to achieve 5ns readout times.
- [19] A. Sah, S. Kundu, H. Suominen, Q. Chen, and M. Möttönen, Decay-protected superconducting qubit with fast control enabled by integrated on-chip filters, *Communications Physics* **7**, 227 (2024).
- [20] E. Jeffrey, D. Sank, J. Mutus, T. F. White, J. Kelly, R. Barends, Y. Chen, Z. Chen, B. Chiaro, A. Dunsworth, *et al.*, Fast accurate state measurement with superconducting qubits, *Physical review letters* **112**, 190504 (2014).
- [21] A. Bengtsson, A. Opremcak, M. Khezri, D. Sank, A. Bourassa, K. J. Satzinger, S. Hong, C. Erickson, B. J. Lester, K. C. Miao, A. N. Korotkov, J. Kelly, Z. Chen, and P. V. Klimov, Model-based optimization of superconducting qubit readout, *Physical Review Letters* **132**, 100603 (2024).
- [22] S. Hazra, W. Dai, T. Connolly, P. D. Kurilovich, Z. Wang, L. Frunzio, and M. H. Devoret, Benchmarking the readout of a superconducting qubit for repeated measurements, *Physical Review Letters* **134**, 100601 (2025), analyzes why standard fidelity ignores leakage in repeated readout cycles.
- [23] J. Heinsoo, S. Krinner, C. K. Andersen, A. Remm, S. Lazar, S. Krinner, and A. Wallraff, Rapid high-fidelity multiplexed readout of superconducting qubits, *Physical Review Applied* **10**, 034040 (2018).
- [24] P. A. Spring, L. Milanovic, Y. Sunada, S. Wang, A. F. van Loo, S. Tamate, and Y. Nakamura, Fast multiplexed superconducting-qubit readout with intrinsic purcell filtering using a multiconductor transmission line, *PRX Quantum* **6**, 020345 (2025).
- [25] C. C. Bultink, M. A. Rol, T. E. O'Brien, X. Fu, S. de Jong, C. Dickel, A. Bruno, N. K. Langford, and L. DiCarlo, Active resonator reset in the nonlinear dispersive regime of circuit qed, *Physical Review Applied* **6**, 034008 (2016).
- [26] M. A. Castellanos-Beltran, K. D. Irwin, G. C. Hilton, L. R. Vale, and K. W. Lehnert, Amplification and squeezing of quantum noise with a tunable josephson metamaterial, *Nature Physics* **4**, 929 (2008).
- [27] C. Macklin, K. O'Brien, D. Hover, M. Schwartz, V. Bolkhovskiy, X. Zhang, W. D. Oliver, and I. Siddiqi, A near-quantum-limited josephson traveling-wave parametric amplifier, *Science* **350**, 307 (2015).
- [28] S. Bugu, Resilience of entanglement-induced coordination in adversarial environments: The team-based quantum sabotage game, *arXiv preprint arXiv:2510.22444* (2025).
- [29] S. Bugu, Hidden-field coordination reveals payoff-free quantum correlation structure in decentralized coordination (2026), *arXiv:2601.21139 [quant-ph]*.
- [30] D. Ristè, C. Bultink, K. W. Lehnert, and L. DiCarlo, Feedback control of a solid-state qubit using high-fidelity projective measurement, *Physical review letters* **109**, 240502 (2012).
- [31] K. T. Goh, J. Kaniewski, E. Wolfe, T. Vértesi, X. Wu, Y. Cai, Y.-C. Liang, and V. Scarani, Geometry of the set of quantum correlations, *Physical Review A* **97**, 022104 (2018).
- [32] B. D'Anjou, Generalized figure of merit for qubit readout, *Physical Review A* **103**, 042404 (2021).
- [33] H. Chernoff, A measure of asymptotic efficiency for tests of a hypothesis based on the sum of observations, *The Annals of Mathematical Statistics* **23**, 493 (1952).
- [34] M. Nussbaum and A. Szkoła, The chernoff lower bound for symmetric quantum hypothesis testing, *Annals of Statistics* **37**, 1040 (2009).
- [35] S. Boutin, C. K. Andersen, J. Venkatraman, A. J. Ferris, and A. Blais, Resonator reset in circuit qed by optimal control for large open quantum systems, *Physical Review A* **96**, 042315 (2017).
- [36] K. M. Audenaert, J. Calsamiglia, R. Muñoz-Tapia, E. Bagan, L. Masanes, A. Acín, and F. Verstraete, Discriminating states: The quantum chernoff bound, *Physical review letters* **98**, 160501 (2007).
- [37] S. Pirandola and S. Lloyd, Computable bounds for the discrimination of gaussian states, *Physical Review A—Atomic, Molecular, and Optical Physics* **78**, 012331 (2008).
- [38] D. Sank, Z. Chen, M. Khezri, J. Kelly, R. Barends, B. Campbell, Y. Chen, B. Chiaro, A. Dunsworth, A. Fowler, *et al.*, Measurement-induced state transitions in a superconducting qubit: Beyond the rotating wave approximation, *Physical review letters* **117**, 190503 (2016).
- [39] Y. Sunada, Y. Kono, S. Wang, Z. Ilves, T. Miyamura, J. Matsuura, S. Tamate, and Y. Nakamura, Photon-noise-tolerant dispersive readout of a superconducting qubit using a nonlinear purcell filter, *PRX Quantum* **5**, 010307 (2024).
- [40] A. Blais, S. M. Girvin, and W. D. Oliver, Quantum information processing and quantum optics with circuit quantum electrodynamics, *Nature Physics* **16**, 247 (2020).
- [41] J. Preskill, Quantum computing in the nisq era and beyond, *Quantum* **2**, 79 (2018).
- [42] A. W. Harrow and A. Montanaro, Quantum computational supremacy, *Nature* **549**, 203 (2017).
- [43] A. Opremcak, C. Liu, C. Wilen, K. Okubo, B. Christensen, D. Sank, T. White, A. Vainsencher, M. Giustina, A. Megrant, *et al.*, High-fidelity measurement of a superconducting qubit using an on-chip microwave photon counter, *Physical Review X* **11**, 011027 (2021).
- [44] T. M. Cover and J. A. Thomas, *Elements of Information Theory* (Wiley-Interscience, 2006).
- [45] E. Rosenthal, C. Schneider, M. Malnou, Z. Zhao, F. Leditzky, B. Chapman, W. Wustmann, X. Ma, D. Palken, M. Zanner, *et al.*, Efficient and low-backaction quantum measurement using a chip-scale detector, *Physical Review Letters* **126**, 090503 (2021).
- [46] R. Barends, J. Kelly, A. Megrant, D. Sank, E. Jeffrey, Y. Chen, Y. Yin, B. Chiaro, J. Mutus, C. Neill, *et al.*, Coherent josephson qubit suitable for scalable quantum integrated circuits, *Physical review letters* **111**, 080502 (2013).

- [47] C. C. Bultink, M. Rol, T. O'Brien, X. Fu, B. Dikken, C. Dickel, R. Vermeulen, J. De Sterke, A. Bruno, R. Schouten, *et al.*, Active resonator reset in the non-linear dispersive regime of circuit qed, *Physical Review Applied* **6**, 034008 (2016).